LAWRENCE
LIVERMORE
NATIONAL
LABORATORY

LLNL-JRNL-422898

Searching for Illicit Materials using Nuclear Resonance Fluorescence Stimulated by Narrow-band Photon Sources

Micah S. Johnson, Dennis P. McNabb, Christian A Hagmann, James M. Hall, John H. Kelley, C. Huibregste, Elaine Kwan, Gencho Rusev, Anton Tonchev

January 26, 2010

Nuclear Instruments and Methods in Physics Research Section B: Beam Interactions with Materials and Atoms

Disclaimer

This document was prepared as an account of work sponsored by an agency of the United States government. Neither the United States government nor Lawrence Livermore National Security, LLC, nor any of their employees makes any warranty, expressed or implied, or assumes any legal liability or responsibility for the accuracy, completeness, or usefulness of any information, apparatus, product, or process disclosed, or represents that its use would not infringe privately owned rights. Reference herein to any specific commercial product, process, or service by trade name, trademark, manufacturer, or otherwise does not necessarily constitute or imply its endorsement, recommendation, or favoring by the United States government or Lawrence Livermore National Security, LLC. The views and opinions of authors expressed herein do not necessarily state or reflect those of the United States government or Lawrence Livermore National Security, LLC, and shall not be used for advertising or product endorsement purposes.

Searching for Illicit Materials using Nuclear Resonance Fluorescence Stimulated by Narrow-band Photon Sources.

M.S. Johnson
Lawrence Livermore National Laboratory, Livermore, CA, 94550
San Jose State University, San Jose, CA, 95192

C.A. Hagmann, J.M. Hall, D.P. McNabb
Lawrence Livermore National Laboratory, Livermore, CA, 94550

J.H. Kelley, C. Huibregtse
North Carolina State University, Raleigh, NC 27695

E. Kwan[1], G. Rusev, A.P. Tonchev[1]
Duke University, Durham, NC 27708

Abstract

We report the results of an experimental study of the sensitivity of two distinct classes of systems that exploit nuclear resonance fluorescence (NRF) to search for illicit materials in containers. One class of systems is based on the direct detection of NRF photons emitted from isotopes of interest. The other class infers the presence of a particular isotope by observing the preferential attenuation of resonant photons in the incident beam. We developed a detailed analytical model for both approaches. We performed experiments to test the model using depleted uranium as a surrogate for illicit material and used tungsten as a random choice for shielding. We performed the experiments at Duke University's High Intensity Gamma Source (HIGS). Using the methodology we detail in this paper one can use this model to estimate the performance of potential inspection systems in certifying containers as free of illicit materials and for detecting the presence of those same materials.

Introduction

Systems to interdict the transport of contraband such as special nuclear materials (SNM) are currently being developed to improve the throughput of choke point screening procedures as part of a multi-layered approach to enhancing national and international security [1, 2]. There are several challenges that need to be met in order to make these technologies broadly useful. Systems need to be flexible enough to search for a broad range of illicit materials, reliable enough to limit false alarms to manageable levels and be capable of scanning large containers and vehicles in time scales of seconds to minutes, all while maintaining reasonably safe radiological dose levels. Nuclear resonance fluorescence (NRF) has been proposed as a physical process that might prove useful in this

[1] Present address: *Lawrence Livermore National Laboratory, Livermore, CA, 94550*

regard, specifically for the detection of fissile materials [3, 4]. NRF (analogous to normal atomic fluorescence) is a process in which a photon at a resonant frequency for a given nucleus interacts with and excites the nucleus. The excited nucleus then decays to its ground state via either direct or multiple transitions. For actinides, these excitations are believed to be either magnetic dipole oscillations such as scissors mode (*cf.* [5]), or electric dipole oscillations assumed to be from octupole-quadrupole vibrations or some other mode. NRF frequencies vary with isotope, thereby providing unique signatures for many materials, and the natural line-widths of the resonances are quite narrow (~ few eV) compared with nuclear level spacings (~100 keV), so accidental interferences between different materials are unlikely, especially when high-resolution detectors are being used. Morover, empirical evidence indicates that overlapping is unlikely. Since NRF states are typically stimulated with MeV-scale photons and the integrated cross sections tend to be quite large (~ 1-100 eV barns) compared with normal atomic attenuation cross sections, it should be possible to penetrate ~ 100-300 g/cm^2 of typical benign material while maintaining a high sensitivity to illicit materials. With narrow-band gamma-ray sources such as those based on Compton backscattering, the radiological dose delivered to an object under inspection could be substantially smaller than that associated with conventional Bremsstrahlung sources and signal-to-noise levels in detectors could also be improved [6].

There are many potential ways to interrogate cargo and vehicles for contraband such as explosives and special nuclear materials (*cf.* [7]). Systems that combine multiple approaches will likely be used to cover a broad range of possible scenarios, but the natural questions that arise are how to best optimize these systems and how to compare the effectiveness of different detection schemes. These can be complex issues to address, particularly given the expectation that actual inspection systems in the field will detect nothing (*i.e.* obtain null results) in the vast majority of cases.

The particular case that we will address here is that of quasi-monoenergetic photon sources stimulating NRF. Data for a variety of scenarios will be used to benchmark an analytical model of performance for two types of systems over a broad range of different scenarios. One class of systems is based on the direct detection of NRF photons emitted from isotopes of interest. The other class infers the presence of a particular isotope by observing the preferential attenuation of resonant frequency photons in the incident beam. For each class of systems we will use the model to estimate the statistical accuracy of a decision metric for a broad set of hypothetical cargo scenarios and the time that it would take to decide on the disposition of the cargo (*i.e.* pass vs. alarm).

The paper begins by reviewing the basic detection protocols for both classes of NRF systems in the next section. The section titled **Classification of threat scenarios** highlights our approach to describing the phase space of possible threats to be detected or excluded. Our approach to modeling system performance is described in the section titled **Analytical model of signals and backgrounds**, followed by sections on the model validation experiments, results and our conclusions.

NRF detection protocols

Protocols for detecting threat materials via their NRF signatures using both reflection- and transmission-based NRF detection schemes have already been discussed in the

literature [4]; however, we will review the fundamentals of a relatively simple, yet robust, set of "operational" protocols here for completeness.

Reflection

In reflection-based detection schemes, the high-energy photon spectrum emerging from the cargo is recorded by an array of detectors located upstream from the cargo and oriented at backward angles to the incident photon beam, where backgrounds from beam-related Compton scattering and other processes tend to be at lower energies than the NRF emission lines from materials of interest. Several millimeters of attenuating material are usually placed in front of these detectors in order to reduce the background count rates to acceptable levels. The rate of beam-induced NRF counts from the cargo is then compared to the rate of transmitted (unattenuated) photons recorded by a beam flux monitor located downstream from the cargo (although perhaps not intuitive, the *transmitted* photon rate is typically used here rather than the *incident* photon rate in order to avoid the possibility of inadvertently failing to detect a threat simply because the surrounding (nominally benign) cargo was too thick for the incident beam to penetrate).

The decision metric (r) for these schemes will be defined as

$$r = \frac{R_{NRF}}{R_T} = \frac{R_S - R_B}{R_T} , \tag{1}$$

where R_S, R_B and R_T are the total signal, background and transmitted count rates, respectively. In contrast to the conventional approach of using "Receiver-Operator Characteristic" (ROC) curves to define the probability of detecting a threat versus the probability of false alarm for *specific* threat scenarios, we will use key values of the decision metric, r, to calculate the "times to decide" (*i.e.* pass vs. alarm) for *arbitrary* cargos at fixed probabilities of false negative (PFN) and false positive (PFP).

The first of the key decision metric values required for the analysis will be r_0, the expected value of r for a completely benign cargo (no trace of threat material). For reflection-based detection schemes, r_0 will be zero since $R_{NRF} = 0$. The second key metric value will be r_2, the expected value of r for a threat cargo. The value of r_2 will depend on both the "minimum credible threat" (MCT) of interest *and* its shielding in this case; however, it will always be $> r_0$. The third key metric value will be r_D, a user-defined boundary between relatively "clean" and relatively "dirty" cargos (*i.e.* between benign cargos which contain relatively small vs. relatively large trace quantities of the threat material, respectively) that will allow us to avoid discontinuities in the "time to decide" estimates. For convenience, the value of r_D will be defined here to be midway between r_0 and r_2 . Note that the value of r_D has no effect on the "time to pass" with a given PFN. Finally, r_2 and r_D will combine with the given values for PFN and PFP to define a fourth key metric value, r_1, which will serve as the effective (operational) decision boundary (pass vs. alarm). The relationship between these key r values is illustrated in Figure 1, where we have used a Gaussian-like distribution to describe the measured decision metric, r_m, and its underlying statistical uncertainty and have indicated the range of r_m values which we will chose to define as "false negative" or "false positive" results.

By using a Gaussian distribution in Figure 1, there will always be a non-zero integral that extends below r_0. We have exaggerated the distribution here so as to not con-

fuse the reader and to be as precise as possible. In practice the distribution will become much more narrow as the integration time increases, such that it will approach a delta-function limit. Therefore the integral below r_0 is negligible. The true distribution will not be a Gaussian but some truncated version that has a sharp cutoff at r_0~0. However, it has been shown by Feldman and Cousins (see Ref. [8]) that the confidence interval for a positively constrained Gaussian is similar to a non-constrained Gaussian, whose mean is sufficiently distinct from zero. This would be the case for typical scenarios implied by this paper and sufficient counting time. Therefore, without loss of generality we use a non-constrained Gaussian distribution to make our model.

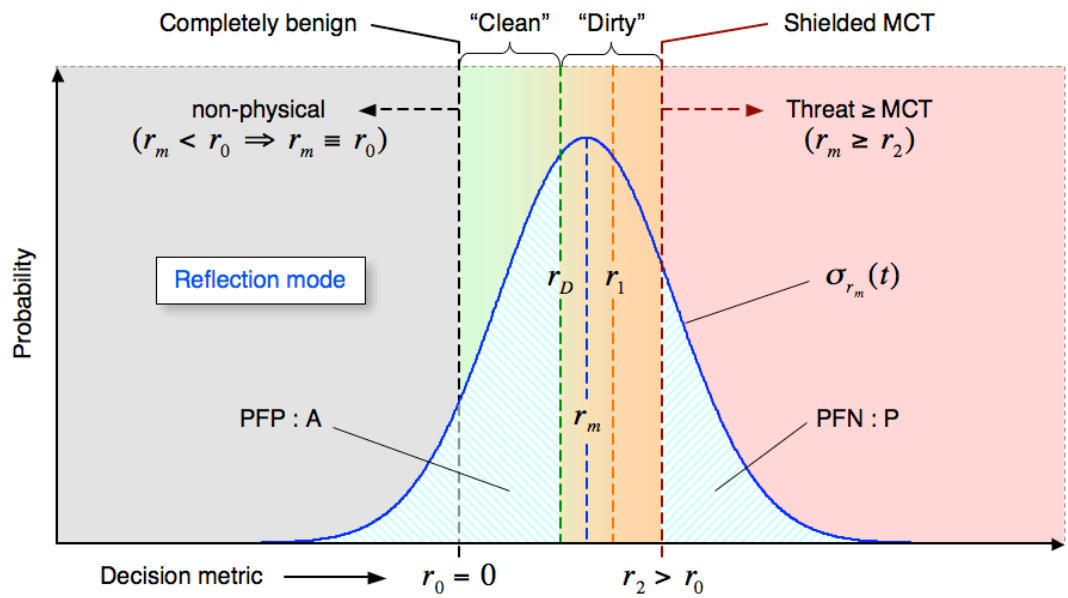

Figure 1: Key decision metric values for reflection-based detection schemes and hypothetical example of measured decision metric, r_m, for a "dirty" cargo after scan time t. Passing a cargo if the true value of r_m is $\geq r_2$ will be defined as a "false negative" result and sounding an alarm if the true value of r_m is $< r_D$ will be defined as a "false positive" result. PFP:A is the probability for false positive if we choose to alarm and PNP:P is the probability for false negative if we choose to pass.

If presented with an unknown cargo to inspect using a reflection-based detection scheme, we will decide on its disposition (pass vs. alarm) based on the final value of r_m relative to r_1. During the course of the scan, the statistical uncertainty in r_m will decrease (*i.e.* the distribution will become more narrow). Referring to Figure 1, it is apparent that, if r_m eventually stabilizes at a value $< r_1$, then the criteria for passing even a somewhat "dirty" (but, by definition, still benign) cargo with a given PFN will be met more quickly than the criteria for sounding an alarm with a given PFP. Conversely, if r_m settles into a value $> r_1$ (indicating either an exceptionally "dirty" cargo or an actual threat). then the reverse will be true. Given this observation, the operational "time to decide" will be defined here as the minimum of the time required to pass the cargo with a given PFN and the time required to sound an alarm with a given PFP.

The time required to pass an unknown cargo will depend on the PFN value used. For the Gaussian-like distribution for r_m shown in Figure 1, the "critical z value" associated with the upper-tail PFN region will be

$$z_{PFN} = \frac{r_2 - r_m}{\sigma_{r_m}(t)} , \tag{2}$$

where $r_m < r_2$ and, neglecting the relatively small uncertainty in R_T (which will always be much less than the uncertainties in either R_S or R_B),

$$\sigma_{r_m}(t) = \frac{\sqrt{(R_S + R_B)}}{R_T \sqrt{t}} = \frac{\sqrt{(r_m R_T + 2R_B)}}{R_T \sqrt{t}} = \sqrt{\frac{(r_m + 2R_B/R_T)}{R_T\, t}} . \tag{3}$$

In reflection-based detection schemes, the ratio R_B / R_T will depend on both the MCT of interest *and* its shielding (both intentional and incidental); therefore, Eqn. (3) cannot be reduced any further. Substituting Eqn. (3) into Eqn. (2) and solving for t, the time required to pass the cargo with a given PFN is thus

$$\text{Time (pass : PFN)} = z_{PFN}^2 \left\{ \frac{(r_m + 2R_B/R_T)}{R_T (r_2 - r_m)^2} \right\} , \tag{4}$$

where again r_m is assumed to be $< r_2$. For inspection scenarios in which r_m is observed to be $\geq r_2$ (*i.e.* an actual threat is indicated), the time to pass the cargo with a fixed PFN value will go to infinity.

Using the same approach, the time required to alarm on an unknown cargo will depend on the PFP value used. For the Gaussian-like distribution for r_m shown in Figure 1, the "critical z value" associated with the lower-tail PFP region will be

$$z_{PFP} = \frac{r_m - r_D}{\sigma_{r_m}(t)} , \tag{5}$$

where $r_m > r_D$ and $\sigma_{rm}(t)$ has the same functional form as before (*cf.* Eqn. (3)). Substituting Eqn. (3) into Eqn. (5) and solving for t, we see that the time required to alarm on the cargo with a given PFP can be expressed as

$$\text{Time (alarm : PFP)} = z_{PFP}^2 \left\{ \frac{(r_m + 2R_B/R_T)}{R_T (r_m - r_D)^2} \right\} , \tag{6}$$

where again r_m is assumed to be $> r_D$. For inspection scenarios in which r_m is observed to be $\leq r_D$ (*i.e.* no threat is indicated), the time to alarm on the cargo with a fixed PFP value will go to infinity.

Combining Eqns. (4) and (6), our operational definition for the time required to decide on the disposition of an unknown cargo using a reflection-based NRF detection scheme will thus be

$$\begin{aligned} \text{Time (decide : PFN, PFP)} &= \min\left[\text{Time (pass : PFN)}, \text{Time (alarm : PFP)}\right] \\ &= \min\left[z_{PFN}^2 \left\{ \frac{(r_m + 2R_B/R_T)}{R_T (r_2 - r_m)^2} \right\}, z_{PFP}^2 \left\{ \frac{(r_m + 2R_B/R_T)}{R_T (r_m - r_D)^2} \right\} \right] . \end{aligned} \tag{7}$$

For inspection scenarios in which $r_m < r_1$, the time to pass with a given PFN will be the defining term in Eqn. (7), while for scenarios in which $r_m > r_1$, the time to alarm with a

given PFP will dominate. Scenarios in which $r_m \sim r_1$ will have similar times to pass or alarm and will, in fact, require the longest overall times to decide. The effective operational value of $r_1 = f(r_D , r_2 , \text{PFN}, \text{PFP})$ will be (calculated from the relationship of r_1 to r_2 and r_D using figure 1),

$$r_1 = \frac{z_{PFP}\, r_2 + z_{PFN}\, r_D}{z_{PFP} + z_{PFN}} \ . \tag{8}$$

In an operational setting, estimates for the times to pass and alarm (Eqns. (4) & (6), respectively) would be continuously updated during the course of a scan using the measured r_m, R_B and R_T values. While these estimates would likely exhibit statistical jitter early on, they can be expected to stabilize on a time scale comparable to the final decision time. The key metric value r_2 (the expected value of r for a minimum credible threat cargo) would need to be estimated prior to the scan using either Monte Carlo or detailed analytic models capable of reliably predicting the response of the system to the MCT of interest in a comprehensive range of both intentional and incidental shielding scenarios. A very conservative estimate for r_2, particularly in regard to how the threat is shielded, will be *critical* to the reliability of these types of detection schemes since, if either the amount or the effectiveness of the shielding is underestimated, an actual threat could easily be undervalued or even missed entirely since the threshold for alarm will have been inadvertently set too high.

It should be noted that the R_B values required to estimate the times to pass and alarm when using a reflection-based detection scheme will include not only low-energy, beam-related backgrounds (which are relatively easy to mitigate), but also a potentially wide range of broad-spectrum backgrounds associated with benign, naturally-occurring radioactive materials (NORM) that might also be present in the cargo under inspection. NORM backgrounds will be highly variable and cannot easily be mitigated without interfering with the NRF emission signal itself. Also, the time required to alarm on a given threat using a reflection-based scheme will depend not only on its shielding, but *also* on its location in the container. Threats located closer to the upstream side of the container (*i.e.* closer to the detector array) will require much less time to alarm on than those located closer to the downstream side of the container (*i.e.* farther away from the detector array). The presence of other (benign) materials in the container that might attenuate either the incident beam or the NRF signal photons will likely exacerbate this effect. On average, symmetrically-shielded threats located near the center of a container will be at once the most difficult to detect and the most difficult to exclude if we assume that the inspection procedure involves scanning both sides of the container.

Transmission

In transmission-based detection schemes, the incident photon beam is analyzed *after* passing through the cargo in an effort to detect a potential "notch" at the resonant frequency that might be associated with NRF absorption in a threat hidden in the cargo. This approach is analogous to radiographic imaging, in the sense that the depth of the notch (or "shadow") in the incident beam will be indicative of the aerial density (ρx) of the resonant isotope along the beam path. The notch is typically measured by placing a small "witness foil" of the isotope of interest (*e.g.* a few grams of ^{235}U, ^{239}Pu, *etc.*) downstream from the cargo. High-energy photons emerging from the witness foil are measured

with detectors placed at backward angles (again to mitigate beam-related Compton scattering that might mask NRF emission lines of interest) and several millimeters of attenuating material are again usually placed in front of the detectors to reduce background levels. The rate of beam-induced NRF counts from the witness foil is then compared to the rate of transmitted (unattenuated) photons recorded by a beam flux monitor located further downstream; however, in contrast to reflection-based detection schemes, the observed NRF count rate will be inversely related to the threat level in this case since a *high NRF count rate* coming from the witness foil (due to the absence of a "notch" in the transmitted beam) will imply low resonant absorption in the cargo and, thus, a *low threat probability*, whereas a *low NRF count rate* from the witness foil (due to the presence of a significant a "notch" in the transmitted beam) will imply a high resonant absorption in the cargo and, thus, a *high threat probability*.

The decision metric (r) for these schemes will again be defined as

$$r = \frac{R_{NRF}}{R_T} = \frac{R_S - R_B}{R_T} , \tag{9}$$

where R_S, R_B and R_T are the total signal, background and transmitted count rates, respectively, and we will again forgo defining ROC curves to assess performance for *specific* threat scenarios in favor of using key values of the decision metric, r, to calculate the "times to decide" (*i.e.* pass vs. alarm) for *arbitrary* cargos at fixed probabilities of false negative (PFN) and false positive (PFP).

The first key metric value required for the analysis will again be r_0, the expected value of r for a completely benign cargo (no trace of threat material). For transmission-based detection schemes, r_0 will be a positive constant, α, (defined during the initial system calibration process) which will depend only on the design of the specific system (*e.g.* detector efficiencies, witness foil thickness, *etc.*), *not* on the cargo under inspection (or, indeed, even on the *presence* of a cargo in the incident beam). The second key metric value will again be r_2, the expected value of r for a threat cargo. The value of r_2 will depend only on the "minimum credible threat" (MCT) of interest in this case, *not* on how (or even *if*) it is shielded; however, it will always be $< r_0$. The third key metric value will again be r_D, the user-defined boundary between relatively "clean" and relatively "dirty" cargos (*e.g.* midway between r_0 and r_2). Finally, r_2 and r_D will again combine with the given values for PFN and PFP to define a fourth key metric value, r_1, which will serve as the effective (operational) decision boundary (pass vs. alarm). The relationship between these key r values is illustrated in Figure 2, where we have again used a Gaussian-like distribution to describe the measured decision metric, r_m, and its underlying statistical uncertainty and have indicated the range of r_m values which we will chose to define as "false negative" or "false positive" results.

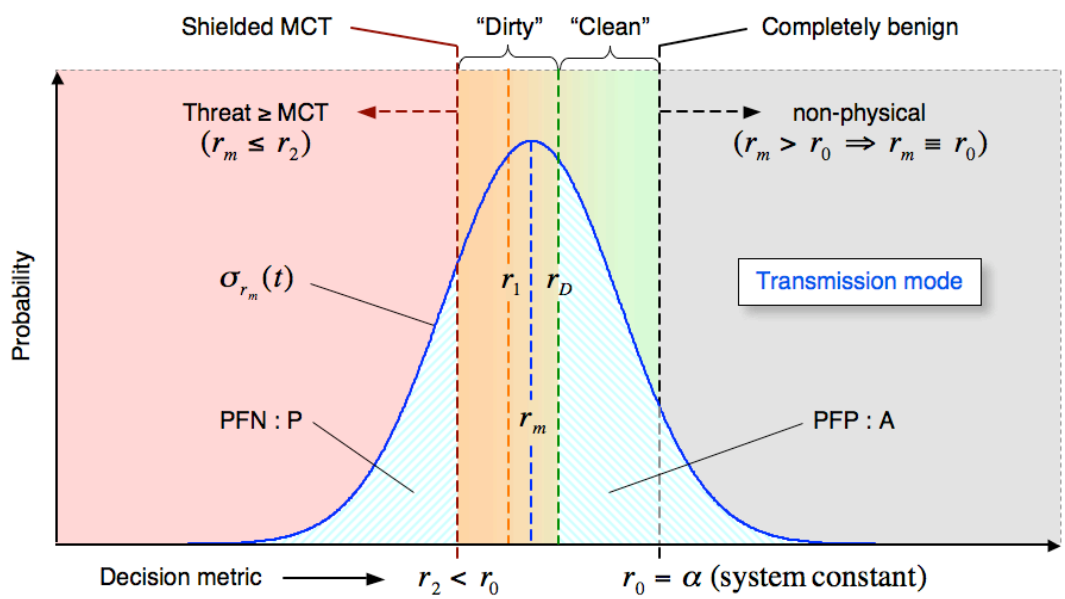

Figure 2: Key decision metric values for transmission-based detection schemes and hypothetical example of measured decision metric, r_m, for a "dirty" cargo after scan time t. Passing a cargo if the true value of r_m is $\le r_2$ will be defined as a "false negative" result and sounding an alarm if the true value of r_m is $> r_D$ will be defined as a "false positive" result. As in Figure 1, PFP:A is the probability for false positive if we choose to alarm and PNP:P is the probability for false negative if we choose to pass.

If presented with an unknown cargo to inspect using a transmission-based detection scheme, we will again decide on its disposition (pass vs. alarm) based on the final value of r_m relative to r_1. Referring to Figure 2 (and keeping in mind that the statistical uncertainty in r_m will again decrease as the scan progresses), it is apparent that, if r_m stabilizes at a value $> r_1$, then the criteria for passing even a somewhat "dirty" (but still benign) cargo with a given PFN will be met more quickly than the criteria for sounding an alarm with a given PFP. If r_m settles into a value $< r_1$ (indicating either an exceptionally "dirty" cargo or an actual threat), then the reverse will be true. Hence, the operational "time to decide" will again be defined as the minimum of the time required to pass the cargo with a given PFN and the time required to alarm with a given PFP.

The time required to pass an unknown cargo will depend on the PFN value used. For the Gaussian-like distribution for r_m shown in Figure 2, the "critical z value" associated with the lower-tail PFN region will be

$$z_{PFN} = \frac{r_m - r_2}{\sigma_{r_m}(t)} , \tag{10}$$

where $r_m > r_2$ and, neglecting the relatively small uncertainty in R_{Tm},

$$\sigma_{r_m}(t) = \frac{\sqrt{(R_S + R_B)}}{R_T\sqrt{t}} = \frac{\sqrt{(r_m R_T + 2R_B)}}{R_T\sqrt{t}} = \sqrt{\frac{(r_m + 2R_B/R_T)}{R_T\, t}} . \tag{11}$$

In transmission-based detection schemes, the ratio R_B / R_T will be a positive constant, β, (also defined during the initial system calibration process) which will depend only on the

design of the specific system, *not* on the cargo under inspection; therefore, Eqn. (11) can be reduced to

$$\sigma_{r_m}(t) = \sqrt{\frac{\left(r_m + 2R_B/R_T\right)}{R_T\, t}} = \sqrt{\frac{\left(r_m + 2\beta\right)}{R_T\, t}} \ . \tag{12}$$

Substituting Eqn. (12) into Eqn. (10) and solving for t, the time required to pass the cargo with a given PFN can thus be expressed as

$$\text{Time (pass : PFN)} = z_{PFN}^2 \left\{ \frac{\left(r_m + 2\beta\right)}{R_T \left(r_m - r_2\right)^2} \right\}, \tag{13}$$

where again r_m is assumed to be > r_2. For inspection scenarios in which r_m is observed to be ≤ r_2 (*i.e.* an actual threat is indicated), the time to pass the cargo with a fixed PFN value will go to infinity.

Using the same approach, the time required to alarm on an unknown cargo will depend on the PFP value used. For the Gaussian-like distribution for r_m shown in Figure 2, the "critical z value" associated with the upper-tail PFP region will be

$$z_{PFP} = \frac{r_D - r_m}{\sigma_{r_m}(t)} \ , \tag{14}$$

where $r_m < r_D$ and $\sigma_{rm}(t)$ has the same final form as before (*cf.* Eqn. (12)). Substituting Eqn. (12) into Eqn. (14) and solving for t, we see that the time required to alarm on the cargo with a given PFP can thus be expressed as

$$\text{Time (alarm : PFP)} = z_{PFP}^2 \left\{ \frac{\left(r_m + 2\beta\right)}{R_T \left(r_D - r_m\right)^2} \right\}, \tag{15}$$

where again r_m is assumed to be < r_D. For inspection scenarios in which r_m is observed to be ≥ r_D (*i.e.* no threat is indicated), the time to alarm on the cargo with a fixed PFP value will go to infinity.

Combining Eqns. (13) and (15), our operational definition for the time required to decide on the disposition of an unknown cargo using a transmission-based NRF detection scheme will thus be

$$\begin{aligned} \text{Time (decide : PFN, PFP)} &= \min\left[\text{Time (pass : PFN)}, \text{Time (alarm : PFP)}\right] \\ &= \min\left[z_{PFN}^2 \left\{ \frac{\left(r_m + 2\beta\right)}{R_T \left(r_m - r_2\right)^2} \right\}, z_{PFP}^2 \left\{ \frac{\left(r_m + 2\beta\right)}{R_T \left(r_D - r_m\right)^2} \right\} \right] . \end{aligned} \tag{16}$$

For inspection scenarios in which $r_m > r_1$, the time to pass with a given PFN will be the defining term in Eqn. (16), while for scenarios in which $r_m < r_1$, the time to alarm with a given PFP will dominate. Scenarios in which $r_m \sim r_1$ will have similar times to pass or alarm and will, in fact, require the longest overall times to decide. For reference, the effective operational value of $r_1 = f(r_D\ , r_2\ ,$ PFN, PFP) will again be (calculated from the relationship of r_1 to r_2 and r_D using figure 2),

$$r_1 = \frac{z_{PFP}\, r_2 + z_{PFN}\, r_D}{z_{PFP} + z_{PFN}} \ . \tag{17}$$

In an operational setting, estimates for the times to pass and alarm (Eqns. (13) & (15), respectively) would be continuously updated during the course of a scan using the measured r_m and R_T values and the system calibration constant, β. While these estimates would again exhibit statistical jitter early on, they can be expected to stabilize on a time scale comparable to the final decision time. The key metric value r_2 (the expected value of r for a minimum credible threat cargo) would again need to be estimated prior to the scan using either Monte Carlo or detailed analytic models capable of reliably predicting the response of the system to the MCT of interest; however, in this case, a single calculation involving only the MCT should be sufficient since (as noted earlier) r_2 will not depend on how (or even *if*) the threat is shielded.

It should be noted that the background levels in the detectors used in a transmission-based scheme should be much more stable and easier to manage than those in a reflection-based scheme since the only material in their field of view is the NRF witness foil (a known quantity) and their shielding can be carefully tailored to minimize potential interference from high-energy photons scattered out of cargo or emitted by the benign witness foil, or NORM that might be present. Also, unlike reflection-based schemes, the time that it takes to detect a given threat using a transmission-based scheme will *not* depend on the location of the threat in the container or on the structural details of its intentional or incidental shielding. It will only depend on the relative amount of NRF resonant absorption that occurs in the incident photon beam as it passes through the container and its cargo (*i.e.* upon "notch" formation).

PFP and PFN values

Finally, we note that the choice of appropriate PFP and PFN values for use with detection schemes such as these will ultimately be driven by the Concept of Operations ("ConOps") used to implement actual systems in the field. Since the consequences of a "false negative" (failing to detect an actual threat) are potentially catastrophic, PFN values are usually set quite low (*e.g.* 10^{-9}) in order to minimize the risk of allowing nuclear material or an actual nuclear device to pass undetected. On the other hand, the consequences of a "false positive" (failing to pass a benign cargo on its first scan) are far less dire (*i.e.* simply back up and repeat the scan), so PFP values are potentially much more flexible (*e.g.* a reasonable ConOps could arguably use a relaxed PFP value ~ 10^{-3} to reduce decision times without incurring significant logistical problems with re-scans); however, the current standard seems to be to use PFP ~ PFN ~ 10^{-9}, so these are the values that we will adhere to for now (*cf.* [9]).

Classification of threat scenarios

In attempting to discuss the relative merits of different detection schemes and methods, not all approaches lend themselves easily to the same classification scheme; however, given the strong similarities between the NRF inspection systems considered in this work and conventional backscatter and radiographic imaging systems, adapting an approach similar to that used for imaging will be useful. The results of our analysis here

could therefore be used to compare NRF systems to other backscatter, radiographic or tomographic techniques employed in search for illicit materials.

One very useful property of laser-driven Compton-backscatter sources with narrow bandwidths is that their beams are highly collimated, typically having divergences of just a few mrad. Given this, we will assume that the thickness of illicit and shielding materials along the beam path does not vary appreciably over the spatial extent of the beam. In other words, variations on a scale smaller than the resolution defined by the beam will not be considered. Also, for the purposes of simplicity, only one region of contraband will be considered in our analysis. Cases where the contraband is split into separate regions or distributed along the beam path are not substantially different in most cases from those in which the SNM lumped together in the middle. In reflection-based systems, spreading the material out along the beam path actually makes detection somewhat easier. In a transmission-based system, distributing the threat material does not affect the depth of the notch in the beam for a fixed aerial density of isotope being irradiated.

Another simplification we will employ here is to ignore spatial variations of the container outside of the incident beam. To the extent that these variations are important for describing signal and background rates, the work presented here can be generalized using tomographic reconstruction for more complex scenarios.

The threat and shielding materials of interest in our scenarios have five relevant physical parameters: density (ρ), thickness (L), atomic attenuation of the beam (μ_a), effective nuclear attenuation on resonance (μ_{NRF}), and cross section for background scattering into the detectors. In the interest of providing concrete numbers, we have taken the threat material to be metallic ^{238}U and the shielding material to metallic tungsten. There is very little loss of generality in these choices. In particular, other shielding materials could easily be substituted for tungsten as long as the thicknesses are chosen to have the same effective overall attenuation and appropriate adjustments are made to account for possible differences in background scattering. Likewise, other threat materials with known NRF states (*e.g.* ^{235}U and ^{239}Pu [10]) will have slightly different values for the attenuation coefficients, but the general trends should be quite similar. Previous measurements indicate that the cross-sections for ^{235}U and ^{239}Pu [10] are not too dissimilar to ^{238}U, therefore, ^{238}U provides a simple and appropriate choice for testing the model. The NRF count rate is proportional to the cross-section, therefore the count time would decrease proportionally (see NRF Protocol section). On the other hand, the "times to decide" (*i.e.* pass vs. alarm) calculated using our analytic model would likely be very sensitive to the detailed characteristics of the photon source (in particular, $\Delta E/E$).

Analytical model of signals and backgrounds

Detailed Monte Carlo simulations were initially used to try to predict the NRF and beam-induced background signals in the detectors used in our experiments at HIGS; however, these simulations quickly revealed several major technical and practical limitations to the Monte Carlo approach. Although COG, the LLNL general-purpose radiation transport code used in the simulations [11], includes NRF absorption and emission models for the actinides of interest in most SNM search scenarios (*e.g.* ^{235}U, ^{238}U and ^{239}Pu), neither it nor any other currently available radiation transport code includes a *complete* model for elastic photon scatter, *i.e.* a model capable of accurately simulating the *coherent combination* of Rayleigh, nuclear Thompson and Delbrück scattering. Figure 3 [12]

shows that transport codes which include only the Rayleigh elastic scattering channel (*e.g.* current versions of COG and MCNP/X) could potentially underestimate beam-induced backgrounds beneath NRF peaks in detectors located at back angles by roughly an order of magnitude at 2176 keV (^{238}U NRF absorption energy).

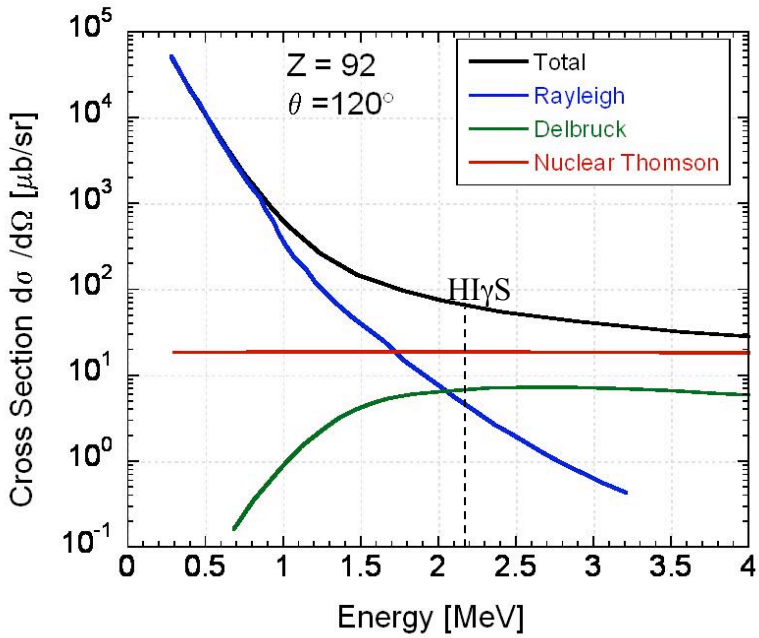

Figure 3: Rayleigh, Delbrück, nuclear Thompson and total elastic scattering cross sections for uranium calculated at 120-degrees [12].

Another serious technical limitation to the Monte Carlo approach involves beam polarization. As will be many Compton backscatter photon sources, the HIGS source is linearly (or circularly, if chosen) polarized, yet none of the currently available transport codes include beam polarization physics (except GEANT [13], which does not contain NRF cross section data in the general distribution). This means that the codes (including COG) might well underestimate NRF yields by factors of 50% or more.

While these technical limitations to the use of Monte Carlo simulations in modeling NRF experiments will eventually be overcome as more advanced transport codes are developed, there will remain practical limitations. Monte Carlo simulations (in particular, those involving the simulation of spectra in high-resolution detectors located at back angles) usually require significant amounts of CPU time to accumulate adequate statistics, even when using high-performance parallel platforms. This can make it very difficult to efficiently explore large, multi-dimensional parameter spaces such as the "time to pass" and "time to detect" for proposed inspection techniques as a function of both the threat and shielding material thicknesses.

As a result of the technical and practical limitations inherent in the Monte Carlo approach, a detailed, analytical model was devised to simulate the HIGS experiments. As was done in Hagmann [9], the HIGS source was modeled as a Gaussian (*cf.* Figure 6) with a peak intensity of ~ 73 photons/eV/sec at 2176 keV (the NRF absorption energy for our surrogate threat, ^{238}U) and a FWHM of ~ 115 keV ($\Delta E/E \sim 0.053$). This source was then decomposed into three "states": (1) N_A, resonant photons in a 6 eV wide bin cen-

tered on the NRF absorption energy (E_A ~ 2176 keV, R_A ~ 438 photons/sec), (2) N_E, non-resonant photons in a 6 eV wide bin centered on the NRF emission line of interest (E_E ~ 22 eV below the NRF absorption energy, R_E ~ 438 photons/sec) and (3) N_H, photons with energies greater than the NRF absorption energy ($\langle E_H \rangle$ ~ 2209 keV, R_H ~ 4.47 x 10^6 photons/sec). Source photons with energies less than the NRF emission energy (*i.e.* below the bounds of the N_E bin) were neglected here since they cannot excite the NRF resonance at ~ 2176 keV in ^{238}U nor can they contribute to beam-induced backgrounds that might interfere with the ^{238}U NRF emission line of interest beyond the resolution width of the HPGe detectors. (Within the resolution width of the HPGe detectors the beam-induced backgrounds from source photons with energies less than the NRF emission energy are not dissimilar to N_E per energy bin given the bandwidth of the beam and the resolution of the detectors, and becomes a negligible effect, *c.f.* discussion below.)

The NRF and beam-induced background count rates in the detectors were calculated for each of the three source photon states (N_A, N_E and N_H) as they propagated through a series of simulated threat objects consisting of various thicknesses of depleted uranium (DU) symmetrically shielded by tungsten (*e.g.* L_W:L_{DU}:L_W). The model utilized standard integral equations with accepted atomic attenuation factors for both incident and generated photons and included detailed treatments of all one- and two-step combinations of NRF, Compton and coherent elastic scattering processes (*i.e.* Rayleigh, Delbrück and nuclear Thompson) capable of either populating or depleting the three source states (note that, while two-step processes are insignificant for thin objects, they can easily contribute 5% or more to the NRF yield from thick objects). Electron-Bremsstrahlung, which could potentially make significant contributions to both NRF yields and elastic backgrounds from thick objects, particularly with high-energy incident photons, was neglected here because the large-angle component of the Bremsstrahlung contributes less than the elastic scatter for the relatively thin objects considered here (*cf.* [14]). Simply multiplying the NRF yields derived from the integral equations by a factor of 1.5 served to approximate beam polarization effects.

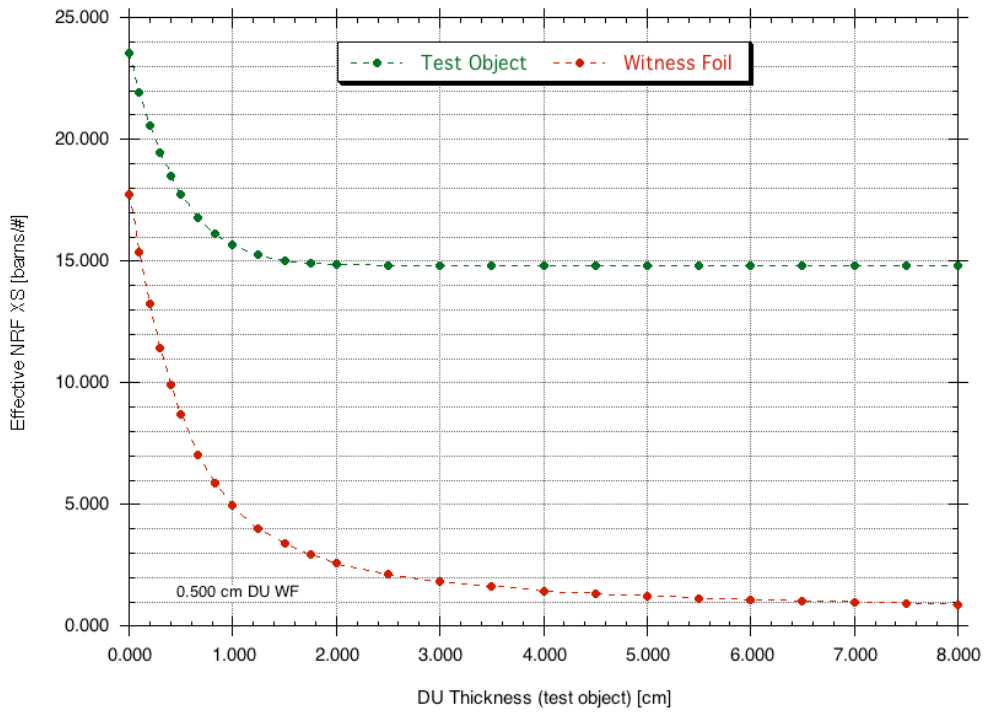

Figure 4: Effective NRF cross section as a function of DU thickness in the test object (green) and witness foil (red). The values shown here were derived by comparing analytic calculations for NRF photon yields done with average cross sections vs. high-resolution, energy-differential cross sections. Note: the witness-foil thickness is constant at 0.5 cm.

A detailed, target-thickness-dependent function was used for the ^{238}U NRF cross section in this model in order to accurately simulate the evolution of the NRF "notch" as the beam passes through the test object and interacts with the witness foil downstream (*e.g.* for transmission-based detection schemes) (cf. Figure 4). The fundamental values for the cross-section can be found in our prior work [9] and references therein. We note that the notch increases in depth until the central region of the resonance structure is completely depleted, after which the effective cross section depends only on the tail regions of the resonance structure. Due to the large separation between the test object and witness foil in our HIGS experiments, forward scattered photons exiting the test object were neglected (*i.e.* "notch filling" was ignored; *cf.* [8, 15]).

Finally, the photopeak detection efficiencies for NRF and back-scattered photons exiting the test object in "reflection" mode and the witness foil in "transmission" mode were estimated using Monte Carlo simulations of the actual HPGe detectors used in the HIGS experiments. The efficiencies derived from these simulations were in close agreement with those measured during the course of the experiment.

Model validation experiments

Schematic cartoons of the experimental setups used to validate our model for NRF reflection- and transmission-mode detection techniques are shown in the upper and

lower frames of Figure 5, respectively. For these measurements, simulated "cargos" of tungsten and surrogate "threats" of depleted uranium (DU) were assembled. Each DU sample was sandwiched between varying thicknesses of tungsten shielding.

In reflection mode (Figure 5, upper), four HPGe detectors (60% efficiency at 1332 keV, relative to a standard 3" x 3" NaI detector) were positioned at backward angles relative to the beam and facing the cargo assembly. In transmission mode, the four detectors were focused on the ^{238}U witness foil (Figure 5, lower). The beam energy was chosen to be 2176 keV to coincide with a prominent NRF absorption resonance in ^{238}U (see [9] and references therein) and the rate was measured at ~ 73 photons/eV/sec at the peak. The FWHM of the beam was ~ 115 keV ($\Delta E/E \sim 0.053$) in this case.

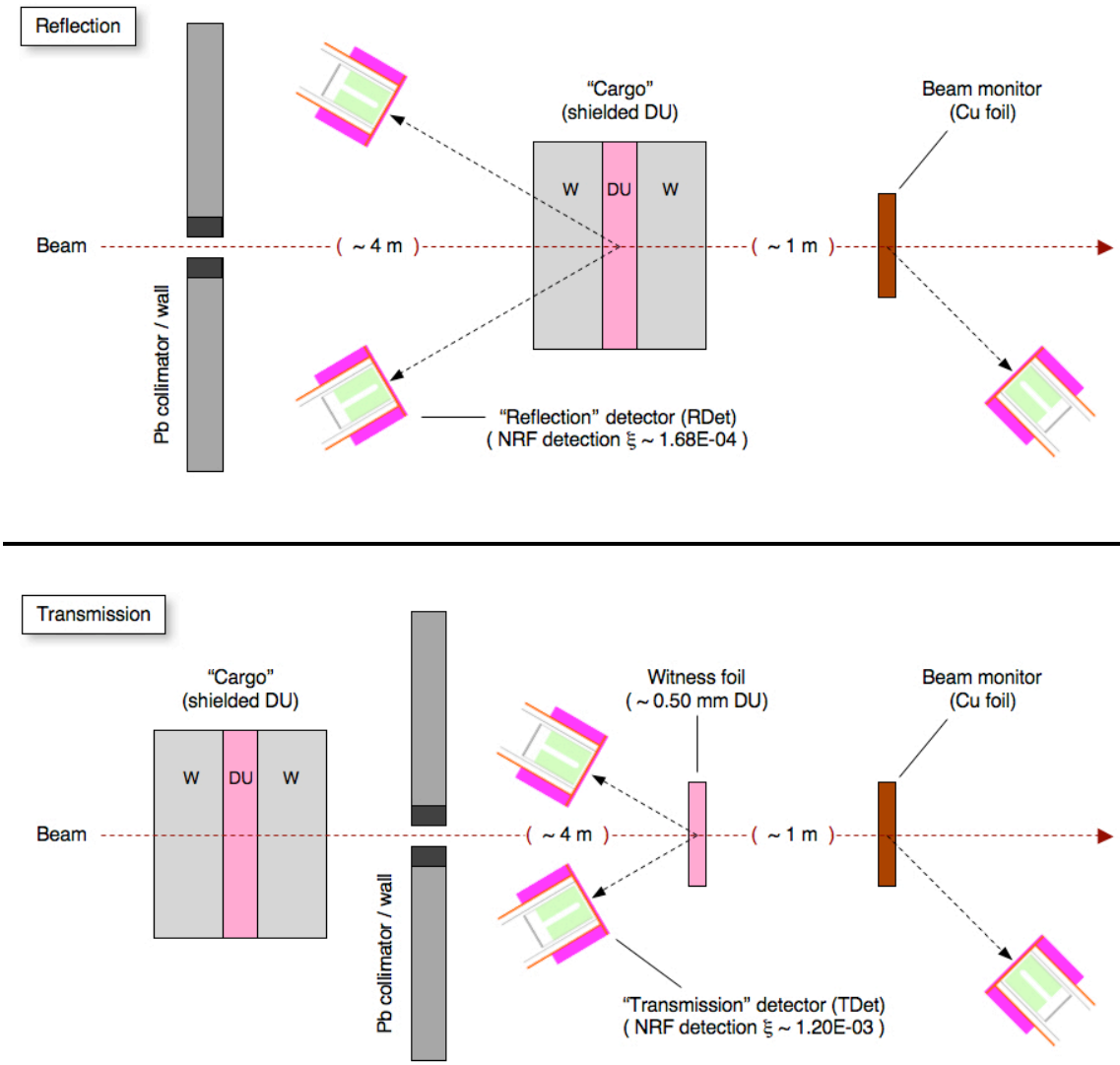

Figure 5: Schematic cartoons of setup for reflection-mode (upper) and transmission-mode (lower) experiments. In both cases, an incident flux of photons impinges on a sample dubbed "cargo". In reflection mode, HPGe detectors are arranged to look at the emission of NRF photons from the cargo. In transmission mode, the detectors are focused on a witness foil made of ^{238}U. In both cases, the transmitted beam is monitored using an HPGe detector that records Compton scatter off of a Cu foil located downstream (beam monitor). Note that this figure is not drawn to scale and is intended only to illustrate the basic experimental

setups. The symbol ξ is the detector efficiency at the NRF energy 2176 keV. The collimator wall consists of 2 meters of concrete and ~ 1 meter of Pb. The interaction point for the Compton backscatter photon source is ~ 80 meters upstream from our experiment. The beam spot is approximately 1 cm diameter and is less than the length and width of the samples and foils.

In reflection mode, two detectors each were positioned at laboratory angles of ~ 130 degrees and ~ 160 degrees with respect to the incident beam. The detector-to-cargo distance was ~ 42.5 cm. Absorbers consisting of 2.4 mm of Pb backed with 4.2 mm of Cu were placed on the front face of each detector in order to suppress beam-induced backgrounds (*e.g*. Compton backscatter). Sleeves of 2.0 cm thick Pb were also placed around the detectors to reduce background from room scatter and other sources. The dead-time was measured to be ≤ 1%.

In transmission mode, two detectors each were positioned at laboratory angles of ~ 100 degrees and ~ 150 degrees with respect to the incident beam. The detector-to-foil distance was ~ 16.4 cm for the smaller angle detectors and ~ 11.4 cm for the larger angle detectors. Absorbers consisting of 9.1 mm of Pb backed with 4.2 mm of Cu were placed on the front face of the smaller angle detectors and absorbers consisting of 5.3 mm of Pb backed with 4.2 mm thick Cu were placed on the front face of the larger angle detectors, again in order to suppress beam-induced backgrounds (*e.g*. Compton backscatter), and sleeves of 2.0 cm thick Pb were again placed around the detectors to reduce background from room scatter and other sources. The DU witness foil used in these experiments was measured to be 5.1 mm thick. The dead-time was measured to be ≤ 1%.

The flux from HIGS was monitored with a single HPGe detector focused on a 1 mm thick Cu foil located on the beam axis downstream of the setup. The HPGe detector measured Compton scattering from the Cu foil at an angle of ~ 13 degrees.

The configurations of simulated "cargos" and surrogate "threats" investigated in our experiments are listed in Table 1 along with the integration times for both detection modes at the HIGS average incident flux of ~ 73 photons/eV/sec (peak). The total flux was about 10^7 photons/sec and is nominally stable to within 5%. The beam spot is approximately 1 cm diameter and is less than the length and width of the samples and foils.

Table 1: Experimental configurations. The first three columns show the thicknesses of W and DU used in the test object (note that the tungsten shielding was applied symmetrically). The live times for each detection mode are also given at the HIGS average incident flux of ~ 73 photons/eV/sec (peak).

Run #	Upstream W [mm]	DU [mm]	Downstream W [mm]	Reflection Livetime [sec]	Transmission Livetime [sec]
1	1.4	1.4	1.4	11885	5829
2	1.4	6.35	1.4	6340	3220
3	1.4	25.4	1.4	8104	3742
4	3.175	1.4	3.175	15611	- - - - -
5	6.35	0.0	6.35	6494	13157
6	6.35	6.35	6.35	30741	10085
7	6.35	12.7	6.35	31260	15133
8	9.525	6.35	9.525	- - - - -	26533

Experimental Results

The gamma ray signals were recorded in histogram mode and the spectra were fit with a simple Gaussian curve on top of a polynomial used to represent the background continuum. The ^{238}U NRF line at 2176 keV was used to provide a signature for the demonstration measurements. The count rates from the 2176 keV peak are listed in Table 2 for the various shielding configurations and detection technique. The uncertainties are dominated by statistical fluctuations and are listed in Table 2. Table 2 also lists a comparison of the predicted count rates (based on the analytical model discussed earlier) alongside the experimental data. The measurements appear to be in agreement with our predictions to within ~ 1 standard deviation in most cases.

Table 2: Count rates [#/sec] for the 2176-keV NRF line from ^{238}U for various threat and shielding configurations and detection modes along with predictions from the analytical model described in the text (the configurations listed here are identical to those listed in Table 1). *The measured value for Run #5 is fit with an area less than zero and is written as strictly zero to guide the eye of the reader.

Run #	Measured Rate (reflection)	Predicted Rate (reflection)	Measured Rate (transmission)	Predicted Rate (transmission)
1	$5.96 \pm 1.93 \times 10^{-3}$	6.68×10^{-3}	$4.87 \pm 1.26 \times 10^{-2}$	5.82×10^{-2}
2	$1.65 \pm 0.47 \times 10^{-2}$	1.39×10^{-2}	$1.58 \pm 0.50 \times 10^{-2}$	1.46×10^{-2}
3	$1.64 \pm 0.46 \times 10^{-2}$	1.53×10^{-2}	$2.41 \pm 3.40 \times 10^{-3}$	5.46×10^{-4}
4	$5.56 \pm 2.25 \times 10^{-3}$	4.88×10^{-3}	(not measured)	4.33×10^{-2}
5	0*	0	$2.74 \pm 0.71 \times 10^{-2}$	4.00×10^{-2}
6	$5.97 \pm 1.70 \times 10^{-3}$	5.78×10^{-3}	$5.11 \pm 1.71 \times 10^{-3}$	6.43×10^{-3}
7	$7.29 \pm 2.03 \times 10^{-3}$	6.27×10^{-3}	$2.25 \pm 0.92 \times 10^{-3}$	1.66×10^{-3}
8	(not measured)	3.28×10^{-3}	$4.54 \pm 1.34 \times 10^{-3}$	3.79×10^{-3}

Figure 6 shows a histogram plot of a typical high-resolution NRF spectrum taken in transmission mode (red) overlaid with a histogram plot of the incident photon spectrum at HIGS (blue). The ^{238}U NRF emission line at 2176 keV is noted.

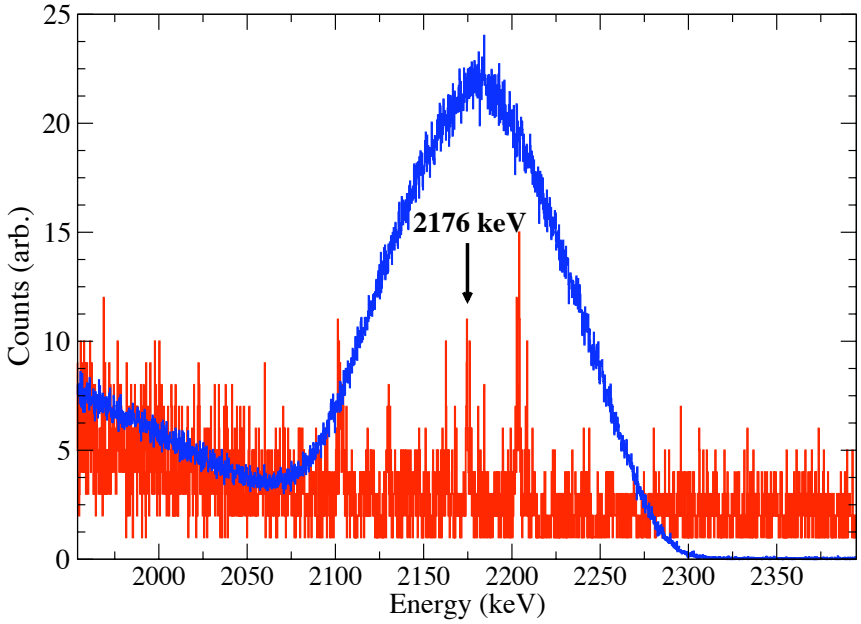

Figure 6: Histogram plot of typical high-resolution NRF spectrum taken in transmission mode (red) overlaid with histogram plot of incident photon spectrum at HIGS (blue). The ^{238}U NRF emission line at 2176 keV is noted.

Contour plots of predicted count rates (counts per second) for the reflection- and transmission-mode setups described above are shown in Figures 7 and 8, respectively, with the experimental configurations listed in Table 1 indicated by black dots. The vertical axis in each case is the total (symmetrically distributed) W shielding thickness. The experimental configurations were chosen with initial guidance from the analytical model. We attempted to use configurations that would test our understanding of predicted gradients *(i.e.* perpendicular to the contours) and variations along iso-contours.

We note that although the effective thicknesses of real cargos will, in many cases be larger than the range shown in the contour plots presented below, it is expected that our analytical model will be valid when extrapolated to real-world values (*e.g.* $\leq \sim 300$ g/cm^2). The truncated phase-space used for the following contour plots was chosen primarily to focus on the test objects used in these feasibility measurements. Furthermore, thin cargos are also of interest.

Figure 7 shows the predicted count rates for reflection mode. As expected, threat materials with the least amount of shielding will have the highest count rate. This is because there is very little material attenuating the NRF signal. Also, as the amount of target material is decreased, the count rate decreases as well since there is less material to produce the NRF signature sought after. The plateau in the contour lines above threat thicknesses of ~ 1 cm is a result of the saturation of measurable counts. This saturation, in turn, is a result of self-shielding effects within the threat material.

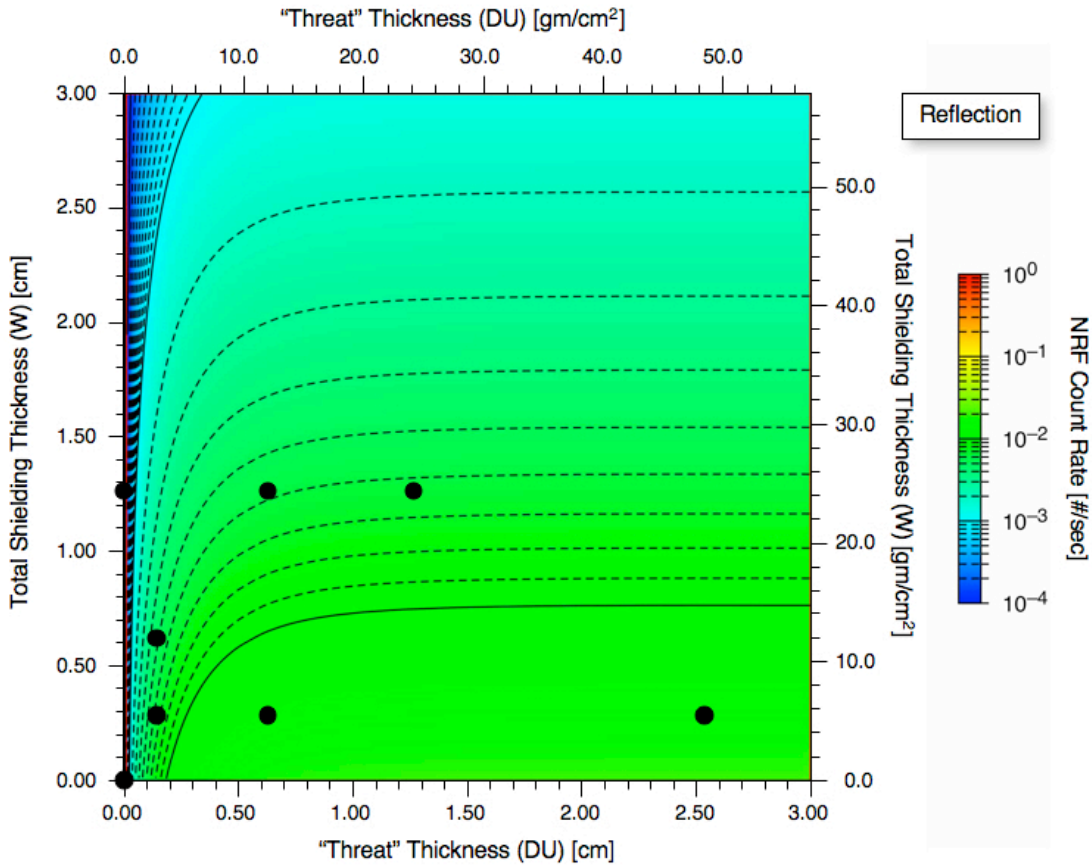

Figure 7: Contour plot of predicted count rates for reflection mode. The contours and color scheme represent predictions made by the analytical model described in the text. The experimental configurations listed in Table 1 are indicated by black dots.

Figure 8 shows the expected count rates for transmission mode. The regions with the lowest count rates are the ones with the highest amounts of shielding and threat thickness. This is expected since the beam is much more highly attenuated in these situations, causing the overall count rate in the transmission detector to decrease.

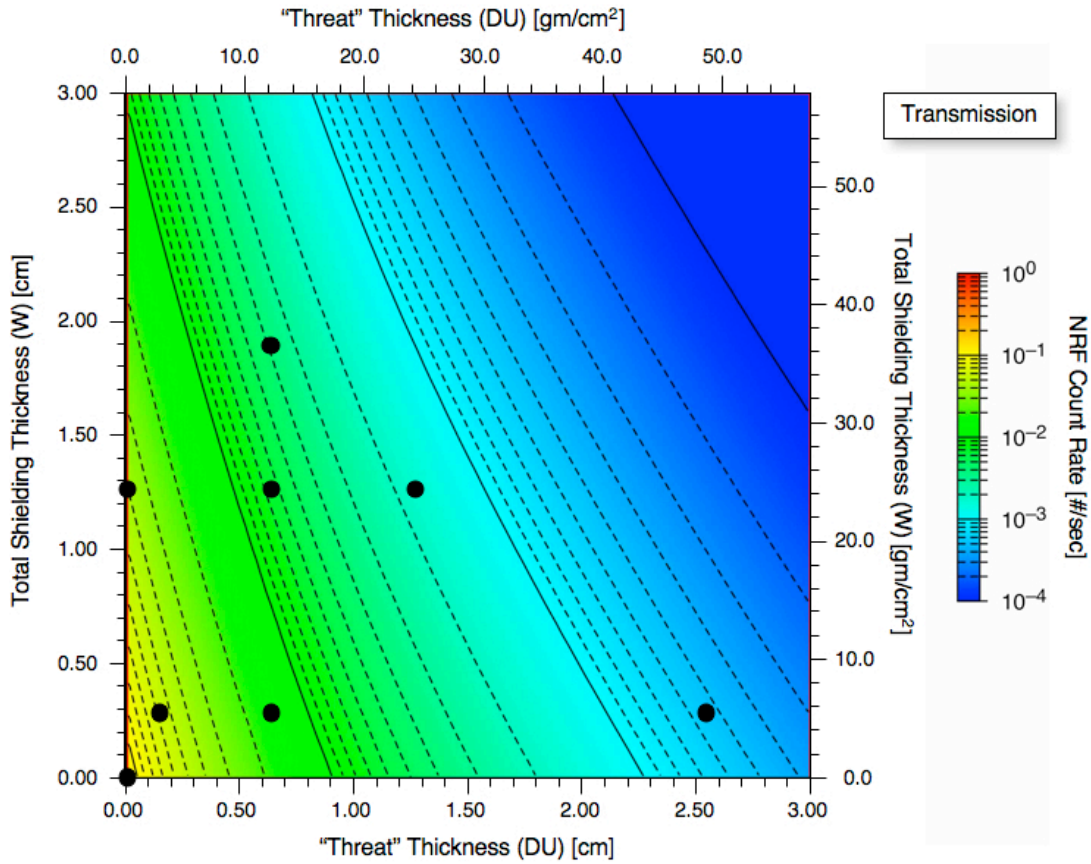

Figure 8: Similar to Figure 5, but for transmission-mode detection experiments.

In order to visualize the agreement/disagreement between the analytical model and the experimental data points, it is necessary to take slices from the plots shown in Figures 7 and 8. We have chosen representative slices along lines with a fixed shielding thickness of 1.27 cm and show the results in Figure 9. The reflection- and transmission-mode data and model predictions are overlaid on each plot in order to facilitate a comparison of the two techniques.

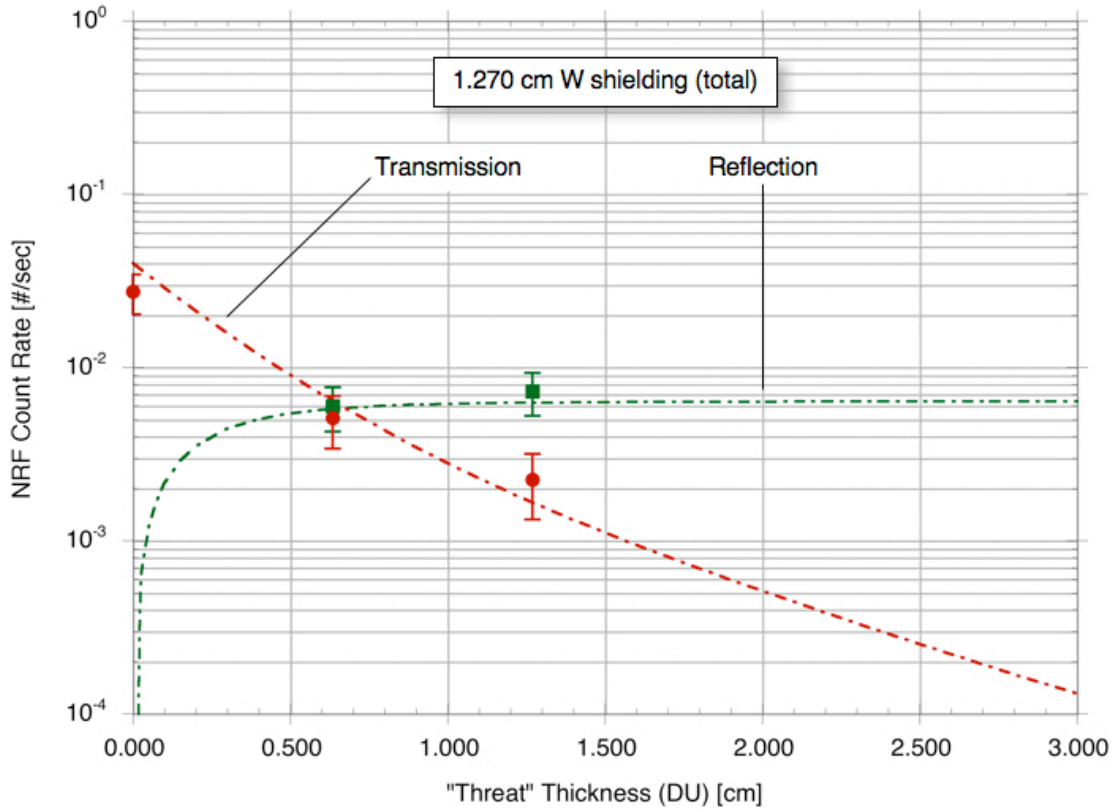

Figure 9: Slice of predicted count rates for 1.270 cm of W shielding (total). The green curve is the prediction for reflection mode and the red curve is the prediction for transmission mode. The data points are the results from our measurements at HIGS with 1.27 cm of total W shielding and various thicknesses of DU (see above description and Table 2.

Given the complexity of the physical processes involved, the agreement between our analytical model and the experimental data points is remarkable, especially considering the fact that the model itself has no free parameters.

Discussion

In Figures 7 and 8, we used our analytical model to produce contour plots of predicted NRF count rates for reflection and transmission, respectively. While count rates are commonly used to compare techniques in the scientific community, in cargo inspection scenarios, a better comparison might be the "time to decide" on the disposition of a cargo (*i.e.* pass with given PFN or sound an alarm with a given PFP) based on some predefined "minimum credible threat" (MCT). In the following discussion, we will use the decision protocols outlined earlier and predicted NRF count rates derived from our analytical model to generate contour plots of the times to decide for random cargos. In line with our experiment, we will define "random cargos" to be arbitrary thicknesses of the threat material (DU in our case) symmetrically shielded by arbitrary thicknesses of W. For the purpose of illustration, the MCT of interest will be arbitrarily defined as 1 cm of DU symmetrically shielded by 2 cm of W (with the shielding arrangement being relevant only in the case of reflection-based schemes) and we will chose confidence levels associ-

ated with 6-sigma statistics (*i.e.* PFN, PFP ~ 10^{-9}). The value r_D was chosen to be 0.5 cm, midway between r_0 and r_2 as suggested in the introduction. Recall from Eq. 8 and 17, the value of r_1 is what becomes important and can be thought of as the centroid of r_D and r_2.

The time to decide on the disposition of a random cargo using a reflection-based detection scheme and a HIGS-type source (~ 73 photons/ eV/sec) is shown in Figure 10, where we have indicated the MCT of interest in its shielded configuration by a light gray dot and have again noted the configurations studied in this experiment by black dots. The cusp that appears in the plot for threat thicknesses between ~ 0.60 cm and 0.80 cm corresponds to cargos which would have measured decision metrics (r_m) roughly equal to the operational pass/alarm decision boundary (r_1). As noted earlier, this is the point at which the time required to pass the cargo with a given PFN will be similar to the time required to sound an alarm with a given PFP. The time to decide is predicted to be relatively short (*e.g.* < ~ 10^4 sec) for scenarios in which the threat material is either relatively thin compared to the defined MCT (*e.g.* < ~ 0.50 cm of DU) or thicker than the defined MCT but relatively lightly shielded (*e.g.* < ~ 1.00 cm of W (total)); however, for even moderately shielded quantities of threat material having r_m values ≥ r_1 (*i.e.* near or above the cusp) it could take an order of magnitude or more longer to decide.

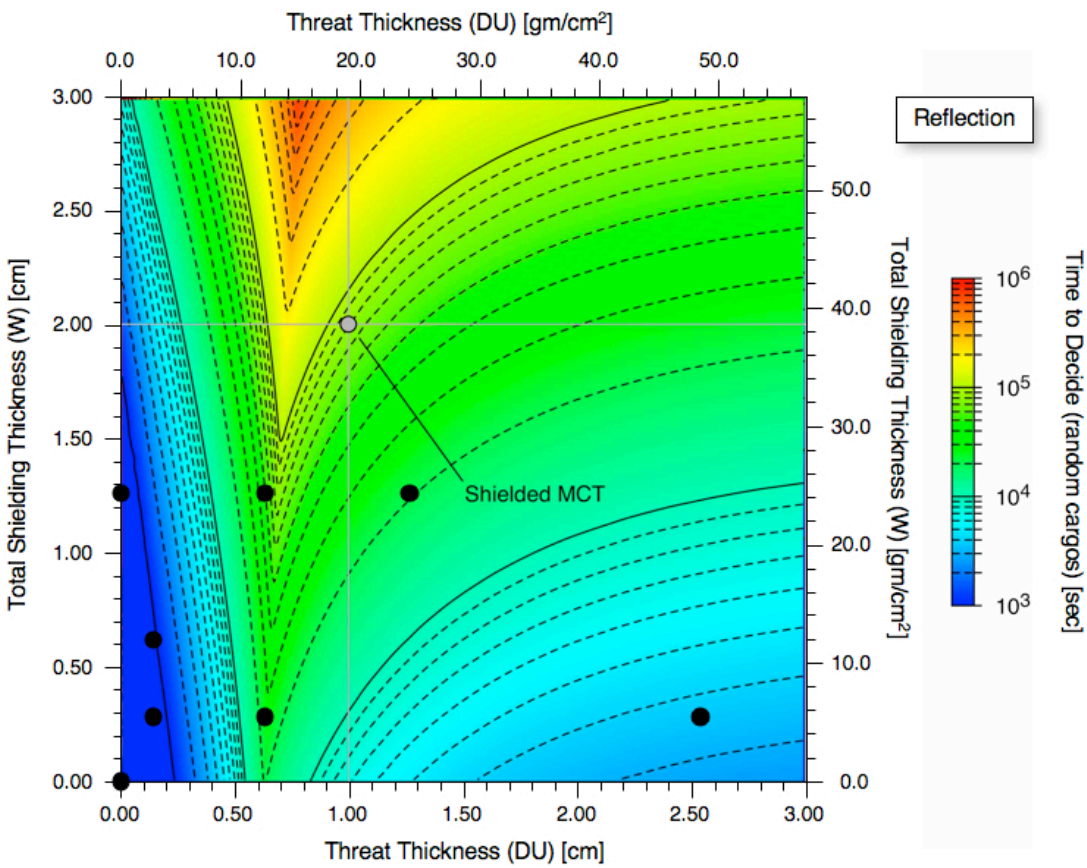

Figure 10: Contour plot of predicted "time to decide" (pass vs. alarm) for a random cargo using a reflection-based detection scheme and a HIGS-type source (~ 73 photons/ eV/sec). The MCT of interest in its shielded configuration is indicated by a light gray dot and the configurations studied in this experiment (*cf.* Table 1) are indicated by black dots. The cusp in the plot corresponds to cargos which would have measured decision metrics (r_m) roughly equal to the operational pass/alarm decision boundary (r_1).

A corresponding plot of the predicted time to decide on the disposition of a random cargo using a transmission-based detection scheme and a HIGS-type source (~ 73 photons/ eV/sec) is shown in Figure 11. The cusp that appears for threat thicknesses ~ 0.50 cm again corresponds to cargos which would have measured decision metrics (r_m) roughly equal to the operational pass/alarm decision boundary (r_1) which, as noted earlier, does not depend on how (or even *if*) the MCT is shielded in this case. The time to decide is again predicted to be relatively short (*e.g.* < ~ 10^4 sec) for scenarios in which the threat material is relatively thin compared to the defined MCT (*e.g.* < ~ 0.40 cm of DU); however, the overall performance of transmission-based schemes for moderately shielded quantities of threat material with r_m values ≥ r_1 (*i.e.* near or above the cusp) is predicted to be far superior to that of reflection-base schemes.

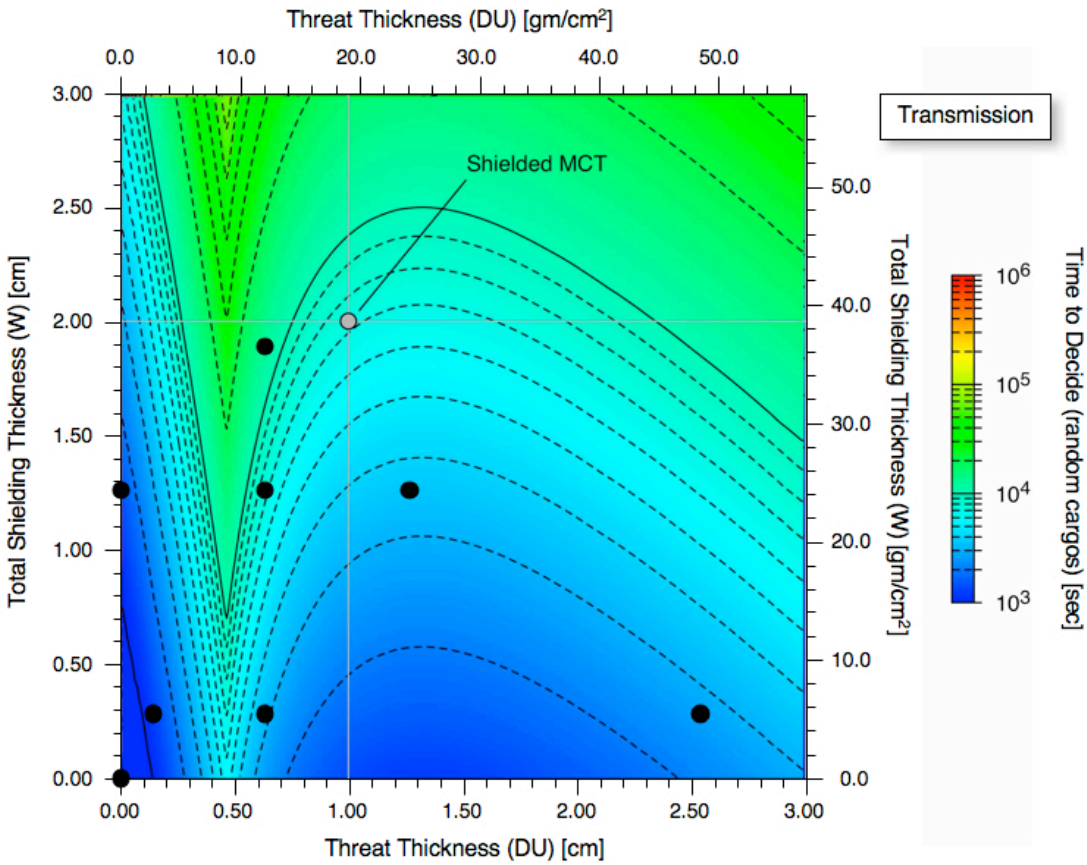

Figure 11: Contour plot of predicted "time to decide" (pass vs. alarm) for a random cargo using a transmission-based detection scheme and a HIGS-type source (~ 73 photons/ eV/sec). The MCT of interest in its shielded configuration (with the shielding being irrelevant in this case) is indicated by a light gray dot and the configurations studied in this experiment (*cf.* Table 1) are indicated by black dots. The cusp in the plot again corresponds to cargos which would have measured decision metrics (r_m) roughly equal to the operational pass/alarm decision boundary (r_1).

Having shown separate plots for the predicted times to decide on the disposition of a random cargo (pass vs. alarm) using reflection-based and transmission-based NRF detection schemes, the most straightforward (and perhaps most insightful) way to compare the overall performance of these two approaches to cargo scanning might be to ex-

amine the ratio of the required times to decide for similar cargo configurations (*i.e.* simply take the ratio of Figure 10 to Figure 11). This ratio is shown in Figure 12, where we have indicated the regions of superior performance (*i.e.* comparatively shorter decision times) for reflection-based and transmission-based schemes by "RDet" and "TDet", respectively. This plot suggests that reflection-based schemes should have better performance for scenarios in which the threat material is relatively thin compared to the defined MCT (*e.g.* < ~ 0.50 cm of DU) and only moderately shielded (*e.g.* < ~ 2.00 cm of W (total)), while transmission-based schemes should work better for a broad range of thicker threats (particularly near and just above the cusp), regardless of how they are shielded. Note, however, that reflection-based schemes are predicted to gain the advantage again for *very* thick threats (*e.g.* > ~ 2.90 cm of DU) with relatively light shielding (*e.g.* < ~ 0.50 cm of W (total)) due to the fact that the incident beam will be heavily attenuated in passing through such cargos (hence requiring somewhat longer times to accumulate sufficient counting statistics at a transmission detector located downstream).

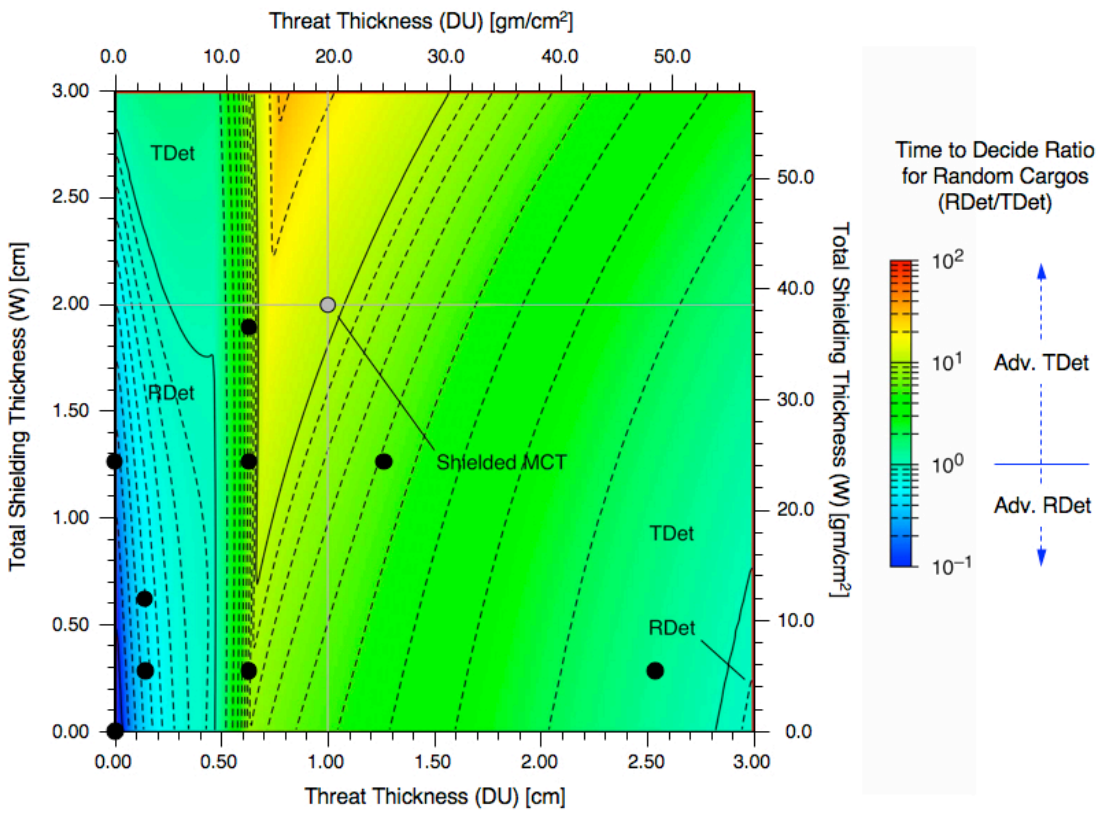

Figure 12: Contour plot comparing predicted "times to decide" (pass vs. alarm) for a random cargo using reflection-based vs. transmission-based detection scheme and a HIGS-type source (~ 73 photons/ eV/sec). The colors and contours in this case represent the ratio of the predictions for reflection-based schemes to those for transmission-based schemes. The regions of superior performance (*i.e.* comparatively shorter decision times) for reflection and transmission are indicated by "RDet" and "TDet", respectively.

It is important to note that, while our analytical model is expected to be valid for the range of surrogate "threats" and simulated "cargos" considered here, it would need to be carefully modified and experimentally validated before using it to model other, more realistic, search scenarios. The detailed predictions for more realistic "threats" and "car-

gos" would undoubtedly differ from those shown here; however (as noted earlier), we believe that the general trends would be similar. Additional analytical models are being considered to simulate different detectors, shielding materials and threats.

Finally, it is worthwhile to re-emphasize the fact that the predicted times to decide discussed above were all calculated for a HIGS-type source (~ 73 photons/ eV/sec at the peak). More advanced, purpose-built Compton-backscatter photon sources such as the Mono-Energetic Gamma-ray ("MEGa-ray") source currently under construction at LLNL [16] are projected to have peak intensities ~ 10,000 times higher than the HIGS beam and would, therefore, provide correspondingly shorter decision times (*e.g.* ~ 1 – 10 sec in most scenarios, using Figures 10 and 11 as guides). This means that the decision as to which type of NRF detection system to use in a given application (reflection-based vs. transmission-based) might ultimately be based primarily on the relative advantages and disadvantages of the techniques noted earlier and their ease of implementation in a particular operational environment. We also note that, while beam-induced backgrounds will increase in proportion to the incident photon flux, this can be at least partially mitigated by using filters that suppress low-energy Compton-backscattered photons relative to photons in the energy region of the beam/NRF state. For example, if Pb filters are used, the attenuation for Compton scattered photons at back-angles (less than 300 keV) is expected to be $\sim 50^x$ greater than the attenuation of the NRF signal (at or near 2.0 MeV), where x is the Pb filter thickness in cm.

Conclusions

We have studied the sensitivity of two distinct classes of systems that exploit nuclear resonance fluorescence (NRF) to search for illicit materials. We have performed experiments to test both approaches in a variety of different scenarios at Duke University's High Intensity Gamma Source (HIGS) and have developed a detailed analytical model that reproduces our results. We have used this model to estimate the performance of potential inspection systems in certifying containers as free of illicit materials and for detecting the presence of those same materials; however, it is clear that more work needs to be done to fully assess the efficacy of reflection- and transmission-mode detection in a wider variety of more realistic threat and shielding scenarios. We note that advances in the design of NRF-based inspection systems could provide the potential to perform high-precision isotopic assay and imaging which, although not explicitly in the mission space of detection, could easily be called for at some point in the future.

References

[1] National Research Council, *Making the Nation Safer: The Role of Science and Technology in Countering Terrorism*, National Academies Press (2002).

[2] J. Medalia, *Detection of Nuclear Weapons and Materials: Science, Technologies, Observations*, Congressional Research Service Report, Library of Congress, Washington, D.C. (2008).

[3] William Bertozzi and Robert J. Ledoux, "Nuclear resonance fluorescence imaging in non-intrusive cargo inspection", NIM B241, 820 (2005); William Bertozzi, Stephen E.

Korbly, Robert J. Ledoux and William Park, "Nuclear resonance fluorescence and effective Z determination applied to detection and imaging of special nuclear material, explosives, toxic substances and contraband", Nucl. Inst. & Meth. B 261, 331 (2007).

[4] J.A. Pruet, D.P. McNabb, C.A. Hagmann, F.V. Hartemann and C.P.J. Barty, "Detecting clandestine material with nuclear resonance fluorescence", J. Appl. Phys. 99, 123102 (2006).

[5] R.F. Casten, *Nuclear Structure from a Simple Perspective*, Oxford University Press, 1990.

[6] R. Hajima, N. Kikuzawa, N. Nishimori, T. Hayakawa, T. Shizuma, K. Kawase, M. Kando, E. Minehara, H. Toyokawa and H. Ohgaki, "Detection of radioactive isotopes by using laser Compton scattered γ-ray beams", Nucl. Inst. & Meth. A 608, S57 (2009).

[7] R.C. Runkle, T.A. White, E.A. Miller, J.A. Caggiano and B.A. Collins, "Photon and neutron interrogation techniques for chemical explosives detection in air cargo: A critical review", Nucl. Inst. & Meth. A 603, 510 (2009).

[8] G. J. Feldman and R. D. Cousins, Phys. Rev. D **57**, 3873 (1998).

[9] C.A. Hagmann *et al.*, "Transmission-based detection of nuclides with nuclear resonance fluorescence using a quasimonoenergetic photon source", J. Appl. Phys. 106, 084901 (2009).

[10] W. Bertozzi, *et al.*, "Nuclear Resonance Fluorescence Excitations Near 2 MeV in ^{235}U and ^{239}Pu", Phys. Rev. C **78**, 041601 (2008).

[11] R. Buck, E. Lent, T. Wilcox and S. Hadjimarkos, *COG: A Multi-particle Monte Carlo Transport Code*, *cf.* http://cog.llnl.gov/.

[12] M. Schumacher, P. Rullhusen, F. Smend, and W. Muckenheim, "THE ENERGY DEPENDENCE OF DELBRUCK SCATTERING INVESTIGATED AT Z = 73,82 AND 92", Nucl. Phys. A **346**, 418 (1980).

[13] GEANT4 Collaboration, Nucl. Inst. & Meth. A506, 250 (2003)

[14] C.A. Hagmann and J.A. Pruet, "Photon production through multi-step processes important in nuclear resonance fluorescence experiments" Nucl. Inst. & Meth. B259, 895 (2007)

[15] B. Quiter *et al.*, "Transmission Nuclear Resonance Fluorescence Measurement of ^{238}U", Nucl. Inst. & Meth. B, doi10.1016/j.nimb.2011.02.081 (2011)

[16] C.P.J. Barty, M.B. Aufderheide, K.S. Budil, G.J. Caporaso, J.M. Hall, F.V. Hartemann, E.P. Hartuni, W.E. King, D.P. McNabb, B. Rusnak, C. W. Siders, J.E. Trebes,

"Precision Mono-Energetic Gamma-ray (MEGa-ray) Science for NNSA Missions", LLNL LDRD 09-SI-004 (2009); C.P.J. Barty, private communication.

Prepared by LLNL under Contract DE-AC52-07NA27344.